energy&fuels

pubs.acs.org/EF

Article

Zr-Modified Ni/CaO Dual Function Materials (DFMs) for Direct Methanation in an Integrated CO_2 Capture and Utilization Process

Seongbin Jo, Jin Hyeok Woo, Tu Nguyen, Ju Eon Kim, Tae Young Kim, Ho-Jung Ryu, Byungwook Hwang, Jae Chang Kim,* Soo Chool Lee,* and Kandis Leslie Gilliard-AbdulAziz*

Cite This: *Energy Fuels* 2023, 37, 19680−19694

Read Online

ACCESS | Metrics & More | Article Recommendations | Supporting Information

ABSTRACT: An integrated CO_2 capture and direct methanation (ICCM) system has recently gained significant attention as a promising process to produce value-added chemicals. Compared to conventional CO_2 capture and utilization, ICCM is a simplified process that directly converts captured CO_2 without purification at lower thermal inputs. One of the primary limitations is the deactivation of the sorbent and the embedded catalysts after several thermal cycles. In this study, we formulated thermally stable macroporous structured Ni/CaO dual function materials (DFMs) by incorporating a Zr stabilizer. The textural properties, porosity, CO_2 capture performance, and catalytic activity of Zr-modified Ni/CaO (Ni/CaZr) were assessed. *In situ* DRIFTS was used to investigate the possible intermediates and reactions during the ICCM. It was found that CH_4 is produced from the formate and methoxy intermediates route on the CaO surface and the CO intermediate route on the Ni surface. Ni/CaZr had improved thermal stability with the best CO_2 capture capacity (13−14 mmol of CO_2/g), CH_4 productivity (13−14 mmol of CH_4/g), CO_2 sorption, and desorption kinetics at 500 °C. The benefit of adding Zr for ICCM enhanced the macroporous structures, which enhanced the CO_2 mass transport and prevented the sintering of Ni and CaO.

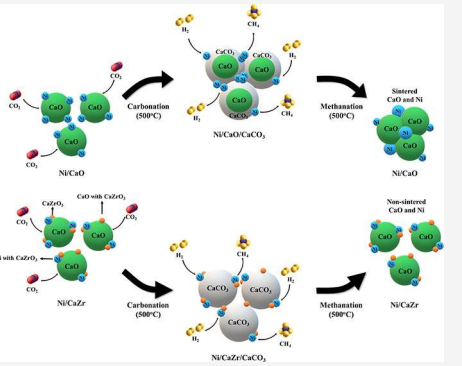

1. INTRODUCTION

Integrated CO_2 capture and utilization (ICCU) has arisen as a promising climate mitigation technology that uses dual function materials (DFMs) to directly transform captured CO_2 into fuels and chemical commodities without the need for separation and purification.[1−13] For conventional CCU, the CO_2 is separated from various waste streams (e.g., flue gas), transported using a pipeline, and transformed into fuels and chemical commodities, in which decarbonation is the most energy-intense process.[2,14,15] For example, CaO sorbent materials capture CO_2 as a formation of $CaCO_3$ at 500−700 °C, and then spent sorbents ($CaCO_3$) are regenerated under condensed or pure CO_2 condition at higher temperatures (∼950 °C), followed by purification to achieve pure CO_2 feedstock. The separated CO_2 is catalytically converted to value-added chemicals. In comparison, ICCU provides a simpler process with lower energetic inputs and has been used to directly transform captured CO_2 without purification of CO_2 feedstock into methanol, synthesis gas, and carbon monoxide.[6] For example, CaO in DFMs captures CO_2, and then the captured CO_2 ($CaCO_3$) directly reacts with H_2 or CH_4 to produce such value-added chemicals or fuels at temperatures lower than decarbonation temperatures.

Among the reactions studied, the CO_2 methanation reaction is one of the simplest and most promising ICCU strategies because of its high conversion and selectivity into methane on a large scale at relatively low temperatures.[16] The CO_2 methanation reaction, $CO_2(g) + 4H_2(g) \leftrightarrow CH_4(g) + 2H_2O(g)$, is exothermic ($\Delta H_{298K} = -165$ kJ/mol), it is thermodynamically limited, and it is favored at low temperatures. Despite high CO_2 conversion and CH_4 selectivity, the slow diffusion of gas limits the overall reaction rate at low temperatures. In contrast, the thermodynamic equilibrium dictates that a high operating temperature will decrease CO_2 conversion and CH_4 selectivity because CO_2 is converted to CO via a reverse water-gas shift reaction, $CO_2(g) + H_2(g) \leftrightarrow CO(g) + H_2O(g)$.[17] Based on the thermodynamic equilibriums ($H_2/CO_2 = 4$), the CO_2 conversion is 98.9% and the CH_4 selectivity is ∼100% at 200 °C, whereas the CO_2 conversion is 71.5% and the CH_4 selectivity is 92.6% at 500 °C. The power-to-gas (P2G) technology transforms surplus power into H_2 via electrolysis.[18,19] The CO_2 methanation converts CO_2 from flue gas and renewable H_2 to produce CH_4.

Our previous paper studied an ICCU-direct methanation (ICCM) process using Ni/CaO DFMs.[9,10] During carbona-

Received: August 5, 2023
Revised: November 13, 2023
Accepted: November 16, 2023
Published: December 7, 2023

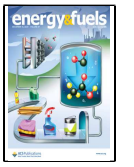

tion, CO_2 is stored by CaO species in the NiO/CaO DFMs as a formation of $CaCO_3$: nNiO/CaO(s) + CO_2(g) ↔ nNiO/$CaCO_3$(s). In the subsequent direct methanation step, NiO is reduced to Ni^0. The captured CO_2 is reactively regenerated using H_2 to form CH_4. The reactive regeneration temperature is much lower than the decarbonation temperature of $CaCO_3$ (~950 °C), with 100% CH_4 selectivity: nNiO/$CaCO_3$(s) + (n + 4)H_2(g) ↔ $n$$Ni^0$/CaO(s) + CH_4(g) + (n + 2)H_2O(g). The exothermic nature of the methanation reaction makes it thermodynamically limited and favorable at low temperatures.[20] All captured CO_2 as a $CaCO_3$ phase was converted directly with H_2 to CH_4 (CH_4 selectivity: ~100%) without CO_2 desorption at 500 and 600 °C. At 700 °C, not all CO_2 was converted with H_2 to CH_4 or CO, leading to low CH_4 selectivity. The optimum reaction temperature was determined to be 500 °C because the Tammann temperature of $CaCO_3$, at which $CaCO_3$ forms large and dense aggregates (sintering), is 533 °C. However, despite the thermodynamically more favorable temperature for CO_2 capture than 600 °C, the experimental CO_2 capture capacity of the catal-sorbents is lower at 500 °C, because of slow diffusion of CO_2 into the active CaO site through the thick layer of $CaCO_3$. In addition, the Ni catalyst and CaO sorbent are still susceptible to sintering (Ni and CaO) and pore shrinkage (CaO).

Therefore, one prime challenge for the ICCU field is developing catalysts and sorbents that maximize CO_2 capture and maintain their inherent activity and selectivity to desired products through frequent temperature fluxes necessary for carbonation and regeneration. For example, calcium oxide (CaO) is one of the most used sorbents for the ICCU process, where it can selectively chemisorb acidic CO_2 to form carbonates (CaO(s) + CO_2(g) ↔ $CaCO_3$(s)). CaO is advantageous because it is relatively inexpensive and has a maximum theoretical CO_2 capture capacity of 17.8 mmol of CO_2/g of CaO.[21−24] The CO_2 capture kinetics of CaO-based sorbents is governed by two reactions: (1) the fast chemisorption of CO_2 with CaO to form $CaCO_3$ and (2) the diffusion of CO_2 through the $CaCO_3$ layer to the free surface of CaO. The thick layer of $CaCO_3$ covers the active CaO particles because of the larger volume of $CaCO_3$ (36.9 cm^3/mol) compared to that of CaO (16.7 cm^3/mol).[22,23,25,26] The volume expansion of CaO-based sorbents during carbonation causes the loss of surface area and pore structures, leading to the severe sintering of sorbents at high temperatures and a drastic reduction of the capture capacity.[24,27] The main reason for the sintering is that the Tammann temperature of $CaCO_3$ (~533 °C) is lower than the operating temperature for carbonation (650 °C) and regeneration (950 °C).[23] Thus, $CaCO_3$ grain sizes will increase, reducing the surface area and pore volume. Ni-based catalysts have been utilized extensively for CO_2 methanation due to their high catalytic activity, high CH_4 selectivity, and low price.[18] At high reaction temperatures, Ni-based catalysts are also susceptible to carbon deposition and sintering.[17,20]

Extensive studies have been conducted to prevent the sintering-induced deactivation of CaO-based sorbents and enhance their multicycle stability.[22,23,28] One of the efficient approaches for sinter-resistant CaO-based sorbents is adding metal oxide stabilizers with high Tammann temperatures, including ZrO_2, SiO_2, Al_2O_3, CeO_2, or MgO. The incorporation of the stabilizers in the CaO structures can enhance the porosity (micro-, meso-, or macro-) and surface area (smaller crystallite size).[23,29−31] The stabilizers can also improve the CO_2 capture capacity and cycle-to-cycle performance by decreasing the CO_2 diffusional path lengths and destruction of the structured morphology by minimizing the volume expansion during the carbonation.[31] One of the most promising stabilizers are Zr-modified CaO to form $CaZrO_3$. The proximity of Zr with the CaO grains at a higher Tammann temperature (1036 °C) increased the cyclic CO_2 capture stability and minimized grain growth or sintering during carbonation and regeneration. Strategies for improving catalyst stability coupled to CO_2-capture sorbents are still developing; however, adding Zr to CaO can also enhance the metal−support interaction between Ni and $CaZrO_3$. For instance, Zhao et al. showed that the NiO crystallites supported on $CaZrO_3$ were smaller, and the reducibility increased due to the stronger metal−support interaction between Ni and $CaZrO_3$.[32]

This study evaluated Zr-modified Ni/CaO (Ni/CaZr) DFMs for the direct methanation process. The key findings show that the addition of ~2% ZrO_2 using the sol−gel method improves the macroporous structure of CaO sorbents, Ni dispersion, and thermal stability of Ni and CaO for up to 30 cycles. The effect of Zr addition as a stabilizer on the performance of the CO_2 capture (capacity and kinetics) was estimated using thermogravimetric analysis (TGA). The experimental data were fitted to the double-exponential model to quantitatively compare the CO_2 sorption kinetics. The influence of Zr addition as a promoter for Ni dispersion on the catalytic activity in CO_2 hydrogenation was evaluated. Mechanistic studies in CO_2 capture and direct methanation in ICCU were determined using *in situ* diffuse reflectance infrared Fourier transform spectroscopy (DRIFTS). Moreover, the long-term stability of the DFMs in CO_2 capture and direct methanation was revealed by using TGA.

2. EXPERIMENTAL SECTION

2.1. DFM Synthesis. Nickel(II) nitrate hexahydrate ($Ni(NO_3)_2$·$6H_2O$), calcium nitrate tetrahydrate ($Ca(NO_3)_2$·$4H_2O$), and zirconium(IV) oxynitrate hydrate ($ZrO(NO_3)_2$·xH_2O) were used as Ni, Ca, and Zr precursors, respectively. Citric acid was used as a chelating agent. Ni/CaO and Zr-modified Ni/CaO (Ni/CaZr) DFMs were fabricated by citrate sol−gel techniques.[9,10,23] Metal precursors and citric acid were dissolved in deionized water, and the solution was vigorously stirred at 50 °C for 1 h. For Ni/CaZr DFMs, the molar ratio of Ca/Zr is 30. Until a dry and porous solid xerogel was formed, the solution was dried in a drying oven overnight at 100 °C. The resulting gel was ground finely and calcined in a furnace at 800 °C for 5 h (temperature ramp rate of 10 °C/min). The resulting DFMs were designated as Ni/CaO or Ni/CaZr. Ni/CaO indicates unmodified DFMs, and Ni/CaZr indicates Zr-modified Ni/CaO DFMs.

2.2. DFM Characterization. The metal contents such as Ni, Ca, and Zr in the DFMs were determined using inductively coupled plasma optical emission spectrometry (ICP-OES). DFMs were dissolved in nitric acid at 200 °C for 1 h. Textural properties such as BET surface area, pore volume, average pore size, and nanoparticle size were estimated from the N_2 adsorption−desorption isotherms at −196 °C using a Micromeritics ASAP 2020 instrument. The average pore size was calculated using the Barrett−Joyner−Halenda (BJH) method. The macroporosity and pore size distribution of the DFMs were measured by a Hg porosimeter (Autopore V 9620). The morphology of the DFMs was determined by using field-emission scanning electron microscopy (FE-SEM, Hitachi, S-4800). The crystalline phase was measured by field-emission transmission electron microscopy (FE-TEM, JEOL, JEM-2100F). H_2 pulse chemisorption was conducted to determine the Ni dispersion and Ni surface area in a quartz tube microreactor (Hiden Analytical CATLAB) combined with an MS spectrometer (Hiden QGA gas analyzer) using 50 mg of DFMs. Prior to the H_2 pulse chemisorption,

https://doi.org/10.1021/acs.energyfuels.3c02935
Energy Fuels 2023, 37, 19680−19694

the DFMs were reduced under 5% H_2/He by increasing the temperature to 500 °C at 10 °C/min and holding for 2 h. The temperature was cooled to 40 °C, and H_2 uptake was obtained in the presence of 5% H_2/He. It was assumed that one hydrogen atom resides on one surface Ni atom, and the cross-sectional area of the Ni atom is 6.49×10^{-20} m^2.[33] H_2 temperature-programmed reduction (H_2-TPR) was used to investigate the reducibility of the DFMs (50 mg) under 5% H_2/He from 100 to 800 °C with temperature ramping of 10 °C/min after pretreatment in He conditions at 800 °C for 1 h in a quartz tube microreactor (Hiden Analytical CATLAB) and MS spectrometer (Hiden QGA gas analyzer). The crystallographic structure of the DFMs was characterized by X-ray diffraction (XRD) analysis (Phillips X'PERT X-ray diffractometer) using a Cu Kα radiation source. The crystallite size of CaO in the DFMs was calculated using the Scherrer equation. The chemical composition of the surface of DFMs was obtained in an X-ray photoelectron spectrometer (XPS) using a NEXSA equipped with an Al Kα source. *In situ* diffuse reflectance infrared Fourier transform spectroscopy (DRIFTS) was done using a Thermo Scientific Nicolet iS10 with a liquid N_2-cooled MCT-A detector. The instrument was fitted with a Harrick Praying Mantis instrument, and about 30 mg of DFM powder sample was loaded into a Harrick HVC-DRM-5 high-temperature cell with ZnSe windows. Spectra were taken with an average of 16 scans per spectrum at 4 cm^{-1} resolution every 30 s. The total flow rate of carrier and reactive gases was fixed at 50 mL/min in all tests. A three-step CO_2 capture, purge, and methanation process was conducted by DRIFTS of Ni/CaZr DFM. The Ni/CaZr DFM was pretreated to in He at 800 °C for 1 h. The reaction temperature was maintained at 500 °C during the three-step process. After reduction of Ni/CaZr DFM, 10 vol % CO_2/He was fed for 30 min (carbonation step), and then pure He was fed to purge CO_2 gas in the cell for 15 min (purge step), followed by a direct methanation step with 50% H_2/He for 90 min. Product gases during the *in situ* DRIFTS were analyzed by an MS spectrometer (Hiden QGA gas analyzer). Additionally, thermogravimetric analysis (TGA) was utilized to estimate the sinter resistance of the DFMs during carbonation and decarbonation (carbonation: pure CO_2 at 650 °C; decarbonation: pure CO_2 at 950 °C) as well as carbonation and direct methanation (carbonation: pure CO_2; direct methanation: pure H_2 at 500 °C).

2.3. Reaction Process. CO_2 hydrogenation was chosen as a probe reaction to determine the effect of Zr addition on the catalytic activity. Ni/CaO and Ni/CaZr DFMs (50 mg) in a quartz tube microreactor (Hiden Analytical CATLAB) were preoxidized to desorb adsorbed gases such as CO_2 and H_2O under pure He at 800 °C for 1 h and then reduced at 500 °C under 5 vol % H_2 for 1 h. After the temperature was cooled to 300 °C under pure He, CO_2 hydrogenation tests were conducted from 300 to 500 °C in 50 °C steps. Product gases during reaction were analyzed by an MS spectrometer (Hiden QGA gas analyzer).

The ICCM process was performed using 0.5 g of DFMs in a stainless reactor (inner diameter of 1/2 in.). The packed-bed reactor was placed in an electric furnace at atmospheric pressure. The reaction temperatures during CO_2 capture and direct methanation were maintained at 500 °C. The N_2 balance gas passed through the vapor generator and then carried water vapor. At the CO_2 capture step, 10 vol % CO_2, 10 vol % H_2O, and balance N_2 flowed through the bed with 40 mL/min of total flow rate. At the immediate methanation step, 90 vol % H_2 and balance N_2 (40 mL/min) were passed after purging the reactor. N_2 was used as the balancing and standard gas. The outlet gases were measured by using a gas chromatograph (GC, Agilent 6890) equipped with two thermal conductivity detectors (TCDs). A Porapak Q packed column was used to separate the N_2, CO_2, and H_2O and during the CO_2 capture step, and the effluent gas was analyzed every 5 min. A Carboxen 1000 packed column was used to separate the H_2, N_2, CO, CH_4, and CO_2 during the direct methanation step, and the effluent gas was analyzed every 10 min.

3. RESULTS AND DISCUSSION

3.1. Characterization. The Ni metal contents of the DFMs (Ni/CaO and Ni/CaZr) obtained by ICP-OES are 9.3, and 9.8 wt %, respectively, which are consistent with the desired metal loading (i.e., 10 wt % Ni) (Table 1). The amount of ZrO_2 in the Ni/CaZr DFM is 1.6 wt %. Zr addition did not affect the BET surface area and nanoparticle size, whereas pore volume increased and average pore size decreased in N_2 adsorption−desorption isotherms (Table S1). In the Hg porosimetry results, the total pore area, average pore size, and porosity of Ni/CaO are 15.8 m^2/g, 657.9 nm, and 74.7%, respectively (Table 1). Notably, Ni/CaZr showed enhanced macroporous structures compared to Ni/CaO: total pore area of 19.3 m^2/g, average pore size of 1254.5 nm, and porosity of 89.2%.

Table 1. Metal Contents and Hg Intrusion Porosimetry Results Such as Total Pore Area, Average Pore Size, and Porosity of the Ni/CaO and Ni/CaZr DFMs

	metal contents (wt %)[a]	total pore area (m^2/g)[b]	av pore size (nm)[b]	porosity (%)[b]
CaO		20.8	1961.1	94.8
Ni/CaO	Ni: 9.3 CaO: 90.7	15.8	657.9	74.7
CaZr		13.0	2297.0	89.3
Ni/CaZr	Ni: 9.8 CaO: 88.7 ZrO_2: 1.6	19.3	1254.5	89.2

[a]Metal contents were obtained by ICP-OES. [b]Total intrusion volume, total pore area, average pore size and porosity were measured by Hg intrusion.

In the SEM images (Figure 1a,b), Ni/CaO DFM has a dense morphology with interconnected structures, whereas numerous cylindrical microstructures were observed in Ni/CaZr DFM. The cylindrical microstructures were not observed in CaO and CaZr (Figure S1). The porosities of CaO, CaZr, Ni/CaO, and Ni/CaZr are 94.8, 74.7, 89.3, and 89.2%, respectively (Table 1). The addition of Ni slightly reduces the macroporosity of CaO (Figure 1a, Figure S1a, and Table 1). The addition of Zr maintains the macroporous structure of CaO even after the addition of Ni (Figures 1b and S1b). These findings indicate a correlation between Zr addition and the formation of macropores. Figure 1c−f illustrates the TEM images and Ni crystallite size distributions of Ni/CaO and Ni/CaZr DFMs. The energy-dispersive spectroscopy (EDS) mapping on the DFMs revealed that Ni nanoparticles of uniform size are dispersed well throughout the CaO in both samples (Figures S2 and S3). Individual Ni particles in Ni/CaO and Ni/CaZr have an average crystallite size of 28.4 and 26.9 nm, respectively, which are relatively smaller than the Ni particle size from XRD results (Figure 1e,f and Table 2). Zr addition improved the Ni dispersion obtained by H_2-pulse chemisorption, which is consistent with a decrease in Ni crystallite size (Table 2). In TEM images of Ni/CaZr DFM, bright small-sized grains (spectra 347) and dark larger-sized grains (spectra 348 and 349) are dispersed throughout CaO (spectrum 350) (Figure S4). Ca, Zr, and O atoms (i.e., $CaZrO_3$) were observed to make up relatively brighter smaller-sized grains, whereas Ni, Ca, Zr, and O atoms, Ni-supported on $CaZrO_3$ phase, make up darker larger-sized grains.

https://doi.org/10.1021/acs.energyfuels.3c02935
Energy Fuels 2023, 37, 19680−19694

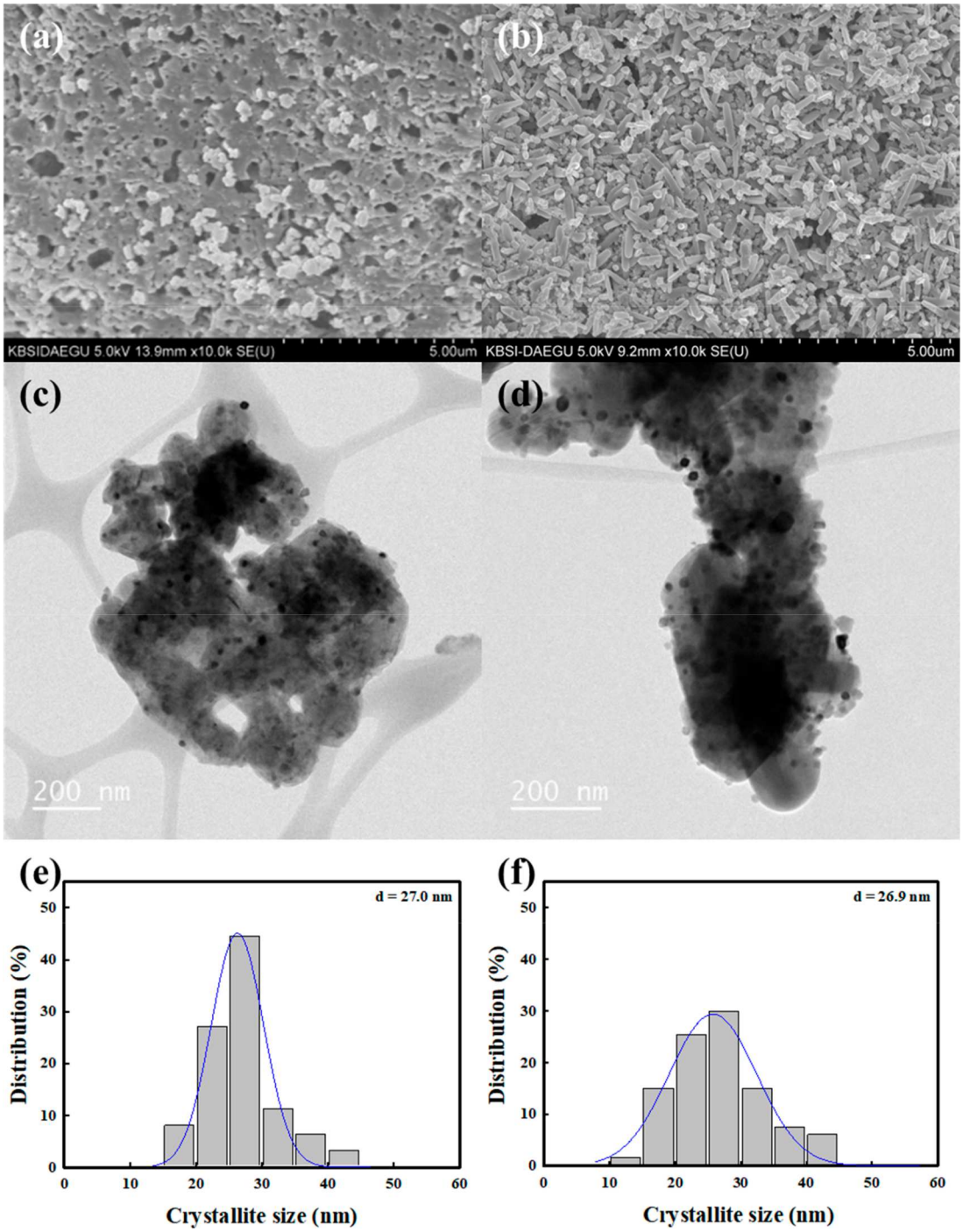

Figure 1. SEM images, TEM images, and Ni crystallite size of the (a, c, e) Ni/CaO and (b, d, f) Ni/CaZr DFMs in the fresh state.

H_2-TPR of Ni/CaO and Ni/CaZr was evaluated under the 5% H_2/He condition from 100 to 800 °C with a temperature ramping of 10 °C/min (Figure 2a). In the H_2-TPR result of Ni/CaO, two overlapped reduction peaks were observed at 400−550 °C. The first peak (α) at ∼480 °C is attributed to the reduction of bulk NiO, indicating minimal or no interaction with the CaO phase, whereas the second peak (β) at ∼530 °C is ascribed to the NiO interacting strongly with the CaO phase. With Zr addition, two reduction peaks (α and β) shifted slightly to higher reduction temperatures because of smaller crystallite size of NiO with a stronger metal support interaction.[34,35] In addition, the third reduction peak (γ) appeared at ∼620 °C, corresponding to the reduction of NiO interacting with Zr species. This indicates that interaction between Ni and Zr species is strong, implying a higher sinter resistance of Ni species in Ni/CaZr DFM, because strong metal−support interaction is recognized as a strategy to prevent the sintering of metal nanoparticles.[36] In Figure 2b, the XRD patterns of the as-prepared Ni/CaO DFM showed CaO (JCPDS No. 48-1467) and NiO phases (JCPDS No. 89-7131). For the as-prepared Ni/CaZr DFM, the Zr is expected to exist as $CaZrO_3$ (JCPDS No. 75-0358) at 31.4°, 45.1°, and 50.8°.[23,37] There were no peaks of ZrO_2 observed, whereas very small peaks of the $CaZrO_3$ (JCPDS No. 76-2401) phase

https://doi.org/10.1021/acs.energyfuels.3c02935
Energy Fuels 2023, 37, 19680−19694

Table 2. Ni Dispersion, Ni Surface Area, and Crystallite Size of the Ni/CaO and Ni/CaZr DFMs

	Ni dispersion (%)[a]	Ni surface area (m^2/g)[a]	crystallite size (nm)
Ni/CaO	3.057	1.885	NiO: 28.4[b]
			NiO: 33.5[c]
			CaO: 50.1[c]
Ni/CaZr	3.579	2.373	NiO: 26.9[b]
			NiO: 28.3[c]
			CaO: 54.5[c]

[a]Ni dispersion and metal surface area were obtained by H_2-pulse chemisorption. [b]Crystallite size of Ni was measured by TEM. [c]Crystallite size of NiO and CaO was calculated by Scherrer's equation from XRD.

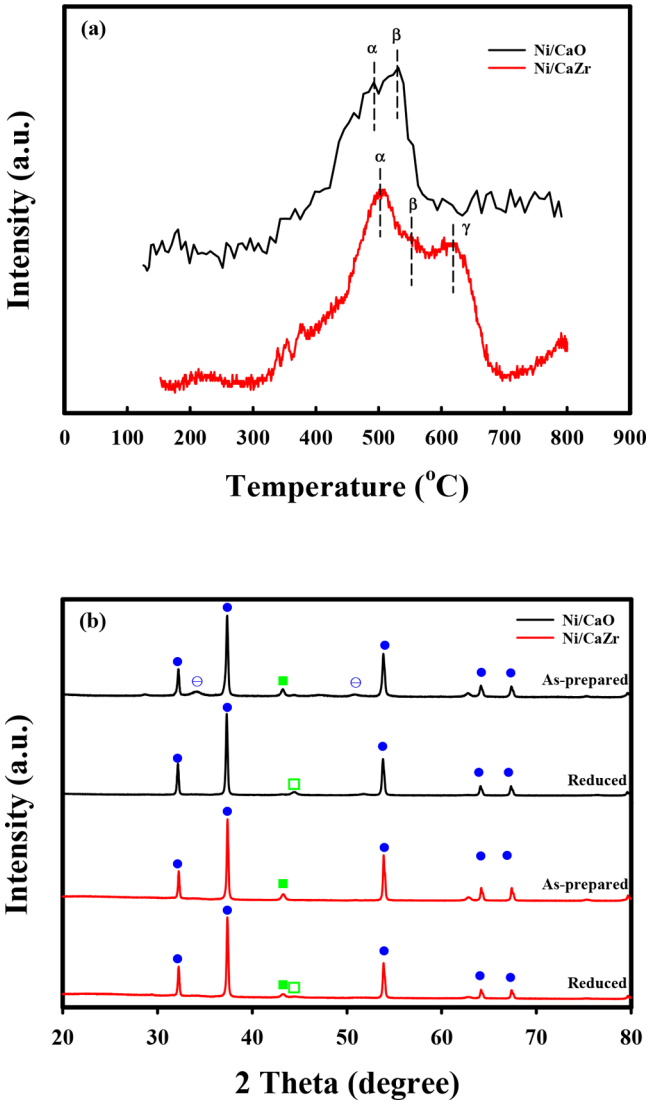

Figure 2. (a) H_2-TPR profiles and (b) XRD patterns of Ni/CaO and Ni/CaZr DFMs in as-prepared and reduced states: (■) NiO and (□) Ni^0; (●) CaO and (⊖) $CaOH_2$.

were observed (Figure S5). We hypothesize that the CaO reacted with ZrO_2 and that the new phase cannot be observed by XRD clearly because of the very low density.[38] The absence of compound $CaZrO_3$ in the XRD analysis could be related to its amorphous form. $CaZrO_3$ has a high Tammann temperature (1218 °C), thermal and chemical stability, and a relatively low thermal expansion coefficient.[39] The formation of $CaZrO_3$ dispersed on the surface of CaO can prevent the aggregation between CaO grains, improving the pore structure. This finding is also corroborated by Yoon et al., who prepared CaO sorbents with a small amount of ZrO_2 (molar ratio of Ca/Zr = 30) using the citrate sol–gel method.[23] The crystallite size of CaO in Ni/CaO and Ni/CaZr DFMs is 50.1 and 54.5 nm, respectively (Table 2). CaO crystallite sizes are comparable regardless of the presence of Zr. The crystallite size of NiO in Ni/CaO and Ni/CaZr is 33.5 and 28.3 nm, respectively. Although these values are greater than the crystallite size obtained by TEM images, the presence of $CaZrO_3$ improves the Ni dispersion. After reduction at 500 °C for 1 h, the NiO peak disappeared, and the Ni^0 peak was observed, indicating a complete reduction of NiO. However, the NiO species is partially reduced to Ni^0 in the Ni/CaZr DFM at 500 °C.

In Figure 3a, the XPS spectra of Ni $2p_{3/2}$ revealed that Ni^{2+} exists in two states within the Ni/CaO and Ni/CaZr DFMs. The C–C component peak located at 284.8 eV was used to calibrate the raw XPS raw data. For Ni/CaO DFM, the peak with the lower binding energy (853.5–854.5 eV) corresponds to the bulk NiO (Ni^{2+} (I)), whereas the peak with the higher binding energy (855.5–856 eV) is attributed to the NiO interacting with CaO (Ni^{2+} (II)),[8] which are consistent with H_2-TPR results. With Zr addition, the proportion of the free NiO, Ni^{2+}(I), decreased slightly from 44.8% to 38.4%, accompanied by an increase in the NiO interacting with CaO, Ni^{2+}(II). This phenomenon results from the smaller size of Ni by Zr addition in the Ni/CaZr DFM. In the Ca 2p spectra (Figure 3b), the Ca $2p_{1/2}$ (350.1 eV) and Ca $2p_{3/2}$ (346.6 eV) were observed with a separation of 3.5 eV and an intensity ratio of 1/2, which is in good agreement with the results reported previously[39]—with the addition of Zr, the binding energy of Ca 2p shifted slightly to the higher binding energy. In the O 1s spectra of Ni/CaO (Figure 3c), Ni/CaO shows the peak at 531.1 eV corresponding to the lattice oxygen of the CaO.[39] On the other hand, Ni/CaZr shows the peak shifted to higher binding energy (531.5 eV) due to the peak overlapping with the oxygen associated with $CaZrO_3$ (532 eV).[39] For Ni/CaZr DFM, the peaks at binding energies of ~181.5 eV (Zr $3d_{5/2}$) and ~184.0 eV (Zr $3d_{3/2}$) correspond to the interaction between Ca and Zr or the formation of the $CaZrO_3$ phase (Figure 3d).[39]

3.2. Effect of Zr Addition on CO_2 Capture Performance (Capacity and Kinetics). Carbonation and decarbonation properties of Ni/CaO and Ni/CaZr were estimated using TGA from room temperature to 1000 °C under pure CO_2 conditions in Figure 4a. For both samples, the onset temperature of CO_2 uptake was approximately 200 °C, and CO_2 uptake increased drastically to 710–730 °C. Both samples achieved the highest CO_2 uptakes of 15.0 and 15.2 mmol CO_2/g CaO, respectively, and then CO_2 is desorbed at a temperature above ~920 °C, which is consistent with thermodynamic equilibrium (Figure S6). Given that the theoretical CO_2 uptake of CaO is 17.8 mmol CO_2/g CaO, theoretical values of Ni/CaO (~90.7 wt % CaO) and Ni/CaZr (~88.7 wt % CaO) are ~16.1 and ~15.8 mmol CO_2/g CaO, respectively. In addition, Ni/CaZr showed higher CO_2 uptake from 200 to 800 °C because better macroporous structures of Ni/CaZr improve the diffusion pathway of CO_2 to CaO active sites. Figure 4b depicts the CO_2 uptake of the Ni/CaO and

https://doi.org/10.1021/acs.energyfuels.3c02935
Energy Fuels 2023, 37, 19680–19694

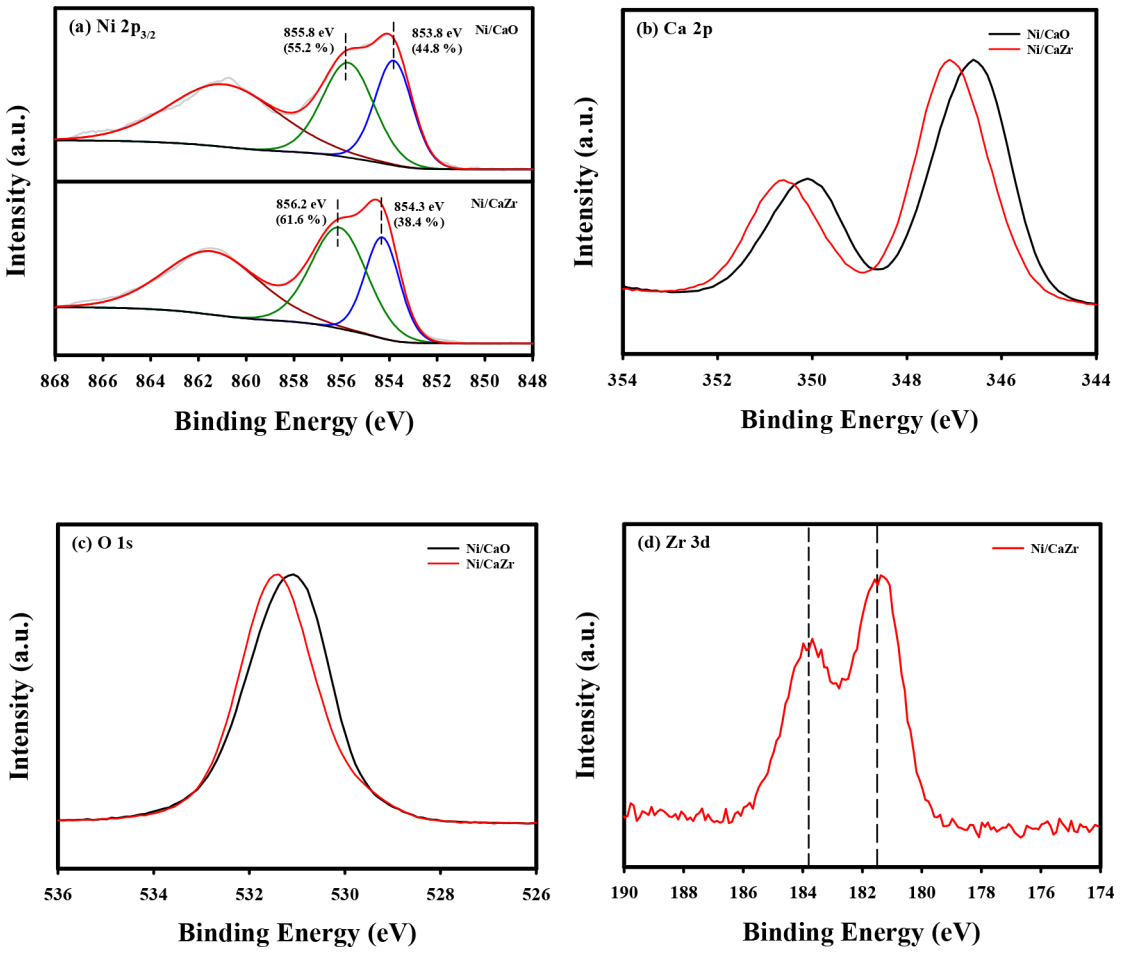

Figure 3. XPS spectra of (a) Ni $2p_{3/2}$, (b) Ca 2p, (c) O 1s, and (d) Zr 3d in Ni/CaO and Ni/CaZr DFMs.

Ni/CaZr DFMs at 500 °C for 80 min under pure CO_2 conditions to evaluate the CO_2 capture performance (capacity and kinetics). The CO_2 uptake of Ni/CaO and Ni/CaZr DFMs at 500 °C was 10.8 and 12.9 mmol of CO_2/g, respectively. The efficiencies of the CO_2 uptake based on the amount of CaO are 67.0% and 81.6% of the theoretical values at 500 °C, respectively. The Ni/CaZr DFMs showed higher CO_2 capture uptake than that of Ni/CaO because the $CaZrO_3$ phase improves the porosity and decreases the diffusional path length for CO_2 to react with basic sites of CaO.

In addition, the TGA curves were fitted to a double-exponential model to compare the overall kinetics of CO_2 uptake quantitatively; these parameters are listed in Table 3.[23] The intrinsic CO_2 adsorption kinetics was not measured.

$$y = A\exp(-k_1x) + B\exp(-k_2x) + C$$

where y represents the weight percent of CO_2 uptake; k_1 and k_2 represent two exponential factors for (1) fast chemisorption and (2) slow diffusion of CO_2 through the $CaCO_3$ layer, respectively. A, B, and C are the pre-exponential factors. For both samples, k_1 values for fast chemisorption (0.2424 and 0.7353 min^{-1}) are greater than k_2 values for slow CO_2 diffusion (0.0201−0.0212 min^{-1}). Although slow CO_2 diffusion through $CaCO_3$ is the rate-limiting step in CO_2 capture, 61.1% of the CO_2 uptake is captured by Ni/CaZr DFM for 2 min. In the literature, CaO sorbent exhibited higher CO_2 uptake than that of Zr-modified CaO sorbent (molar ratio of Ca/Zr = 30) because of higher CaO amount when CO_2 capture was conducted at higher temperatures of 650 °C.[23] However, k_1 values of Ni/CaZr are approximately 3 times higher than that of the Ni/CaO at 500 °C in this study due to the enhanced macroporous structures (>50 nm), corresponding to the Hg porosimetry results such as total pore area, average pore size, and porosity (Table 1). These results mean that gas−solid contact on the CaO surface in the macroporous structure plays an important role in overall CO_2 capture kinetics at relatively low temperatures. On the other hand, k_2 values are comparable regardless of Zr addition, indicating similar CO_2 diffusion through the $CaCO_3$ layer in Ni/CaO and Ni/CaZr DFMs because Zr did not enhance micro- and mesoporous structures (Table S1). Therefore, it is concluded that the enhancement of macroporosity of Ni/CaZr DFM from Zr addition improved the diffusion pathway of CO_2 to CaO active sites, leading to the increase in overall CO_2 capture capacity and kinetics.[40−42]

3.3. Effect of Zr Addition on the Catalytic Activity.

CO_2 hydrogenation was chosen as a probe reaction to determine the effect of Zr addition on catalytic activity. Before the reactions, Ni/CaO and Ni/CaZr DFMs were preoxidized to desorb adsorbed gases such as CO_2 and H_2O under pure He at 800 °C for 1 h and then reduced at 500 °C under 5 vol % H_2 for 1 h. After cooling the temperature to 300 °C under pure He, CO_2 hydrogenation tests were conducted from 300 to 500 °C in 50 °C steps. In Figure 5, CO_2 hydrogenation was evaluated in the steady state for 20 min for each temperature in the presence of 10 vol % H_2 and 10 vol % CO_2. Reaction temperatures increased in 50 °C steps from 250 to 500 °C and

https://doi.org/10.1021/acs.energyfuels.3c02935
Energy Fuels 2023, 37, 19680−19694

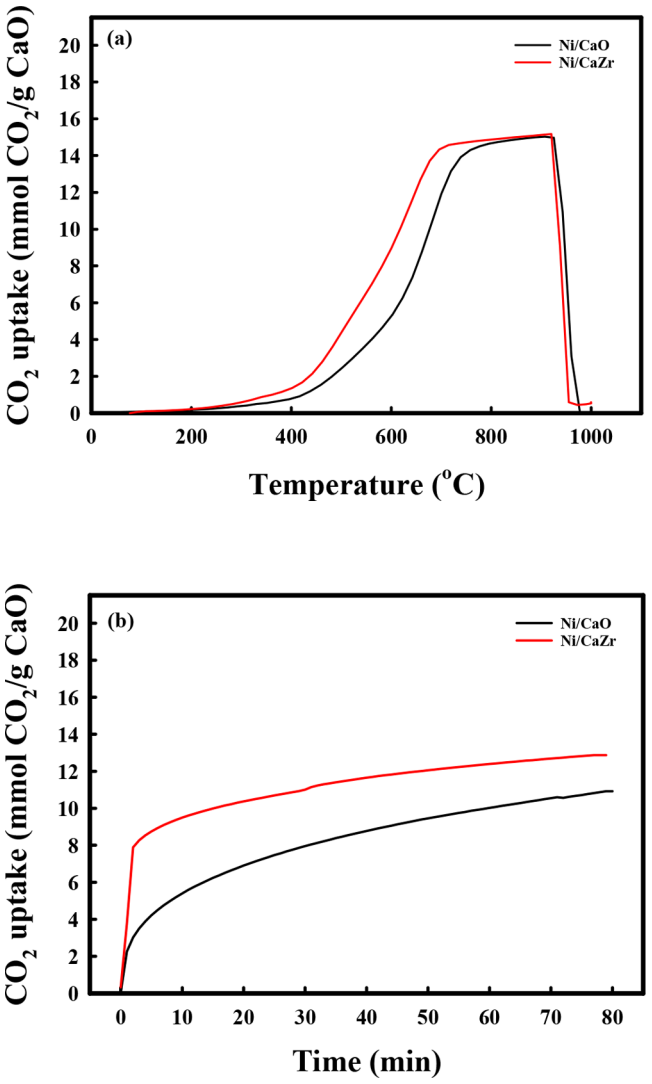

Figure 4. (a) Carbonation and regeneration properties from room temperature to 1000 °C and (b) CO_2 uptake kinetics of Ni/CaO and Ni/CaZr DFMs at 500 °C under pure CO_2 conditions.

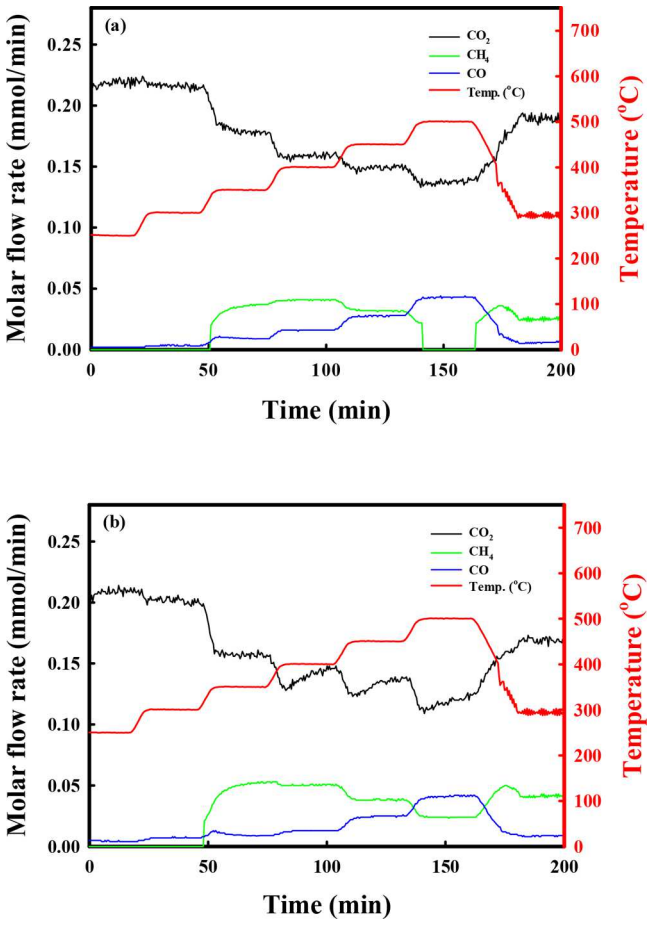

Figure 5. Catalytic activity in CO_2 hydrogenation over Ni/CaO and Ni/CaZr in the presence of 10 vol % CO_2 and 10 vol % H_2.

then cooled to 300 °C. As shown in Figure 5, the onset temperatures over Ni/CaO and Ni/CaZr in CO_2 hydrogenation were 300 and 250 °C, respectively. For both samples, CO_2 was converted to CO without CH_4 production up to 300 °C. CO productivity increased with increasing temperatures, whereas CH_4 productivity increased up to 400 °C for Ni/CaO and 350 °C for Ni/CaZr and then reduced at higher temperatures, which are consistent with thermodynamic equilibria (Figure S7). Although Ni species in Ni/CaZr DFMs were not completely reduced, the conversion of the CO_2 to CH_4 and CO of Ni/CaZr is higher than that of Ni/CaO for all temperatures from 250 to 500 °C because of high Ni dispersion.

3.4. Integrated CO_2 Capture and Direct Methanation.

Consecutive five cycles of CO_2 capture and direct methanation in the ICCU process were evaluated at 500 °C for the Ni/CaO and Ni/CaZr DFMs. CO_2 capture and direct methanation performance were calculated using CO_2 capture breakthrough curves and CH_4 production profiles. The experimental tests were conducted with a low WHSV of 4800 mL/(g h) (0.5 g of DFM at a total flow rate of 40 mL/min) to obtain enough data points for calculation. The low H_2 conversion during the direct methanation step is a limitation by experimental setup (Figure S8). CH_4 productivities for both samples during the five cycles are summarized in Figure 6a, and CO_2 capture breakthrough curves and CH_4 production profiles of Ni/CaO and Ni/CaZr are depicted in Figures 6b and 6c, respectively. There is no CO_2 desorption under N_2 conditions at 500 °C. The captured CO_2 can be directly converted to CH_4 by reacting under H_2 conditions without CO_2 desorption, achieving ~100% CH_4 selectivity, so-called "direct methanation", which was also confirmed by TGA results (Figure S9).[9,10] As can be seen in Figure 6b,c, the breakthrough times of the Ni/CaO and Ni/

Table 3. Kinetic Parameters of the Ni/CaO and Ni/CaZr DFMs Obtained by Fitting the CO_2 Uptake Data to a Double-Exponential Model

	k_1 (min^{-1})	k_2 (min^{-1})	A	B	C	R^2
Ni/CaO	0.2424	0.0201	−11.52	−31.92	51.22	0.9997
Ni/CaZr	0.7353	0.02125	−48.37	−23.98	63.33	0.9882

https://doi.org/10.1021/acs.energyfuels.3c02935
Energy Fuels 2023, 37, 19680−19694

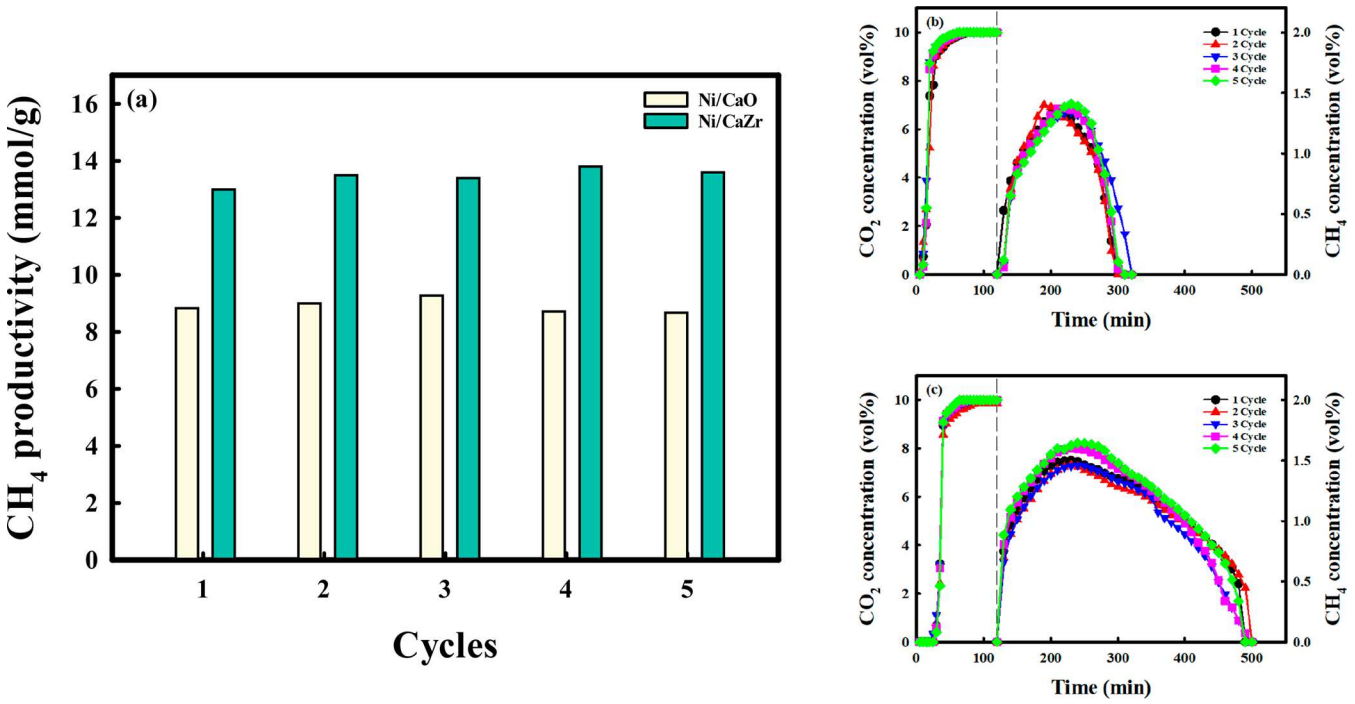

Figure 6. (a) CH_4 productivity of Ni/CaO and Ni/CaZr during five cycles of CO_2 capture and direct methanation at 500 °C. CO_2 capture and direct methanation profiles of (b) Ni/CaO and (c) Ni/CaZr DFMs.

Table 4. CO_2 Capture Capacity of CaO-Based Sorbents or DFMs Reported Previously

DFMs	CaO contents	temp (°C)	feed composition	CO_2 capture capacity (mmol CO_2/g)	ref
Ni/CaZr	88.7 wt %	500	10 vol % CO_2 10 vol % H_2O	13.5	this study
Ni/CaO	90.7 wt %	400	10 vol % CO_2 10 vol % H_2O	7.4	9
		500		9.0	9
		600		15.5	9
		700		16.2	9
$Ca_1Ni_{0.1}Ce_{0.333}$	Ca:Ni:Ce = 1:0.1:0.333	650	15 vol % CO_2	14.1	49
CaO/Ni_4	77.4 wt %	600	100 vol % CO_2	5.7	50
sorbents	CaO contents	temp (°C)	feed composition	CO_2 capture capacity (mmol CO_2/g)	ref
CaZr (c-sg)	Ca/Zr = 30	650	100 vol % CO_2	17.6	23
Ca85Mg15	Ca/Mg = 85/15	650	20 vol % CO_2	14.5	51
CaO	100 wt %	400	100 vol % CO_2	0.96	52
		500		1.19	52
		600		3.26	52
		700		7.78	52
$(Li-K)_2CO_3$/CaO	Ca/$(Li-K)_2CO_3$ = 90/10	400	100 vol % CO_2	4.90	52
		500		6.93	52
		600		10.38	52
		700		10.59	52

CaZr DFMs step were 5 and 25 min, respectively, and CO_2 capture capacities are 8.96−9.75 and 13.2−13.4 mmol CO_2/g, respectively, during the five cycles of carbonation step (Tables S2 and S3). These results mean that Ni/CaZr showed faster kinetics of carbonation and higher CO_2 capture capacities. CH_4 productivities of Ni/CaO during the five cycles were 8.84, 9.01, 9.28, 8.72, and 8.68, respectively. In contrast, Ni/CaZr showed CH_4 productivities of 13.0, 13.5, 13.4, 13.8, and 13.6 mmol CH_4/g during the five cycles (Figure 6a). The CO_2 capture capacity and CH_4 productivity of Ni/CaZr (13.0 mmol CH_4/g) are approximately 1.5 times higher than that of Ni/CaO (8.84 mmol CH_4/g). Ni/CaZr DFM demonstrated the highest CO_2 capture capacity among the CaO-based sorbents or DFMs reported previously (13.0 mmol CO_2/g DFM and 14.7 mmol CO_2/g CaO) at 500 °C, which is 82.3% of the theoretical maximum CO_2 capture capacity (17.8 mmol CO_2/g CaO) (Table 4). The $CaZrO_3$ improved the availability of additional CaO sites, increasing the CO_2 capture capacity and CH_4 productivity. All captured CO_2 by CaO as a formation of $CaCO_3$ can react with H_2 to produce CH_4 without CO_2 desorption (100% CH_4 selectivity), indicating that the CH_4 production capacity is determined by the CO_2 capture capacity. Therefore, the enhancement in the macroporosity

https://doi.org/10.1021/acs.energyfuels.3c02935
Energy Fuels 2023, 37, 19680−19694

of Ni/CaZr DFM led to increases in the CO_2 capture capacity and CH_4 production capacities.

As can be seen in Figure 7, it was determined that the CaO phase in DFMs is converted to $CaCO_3$ following the

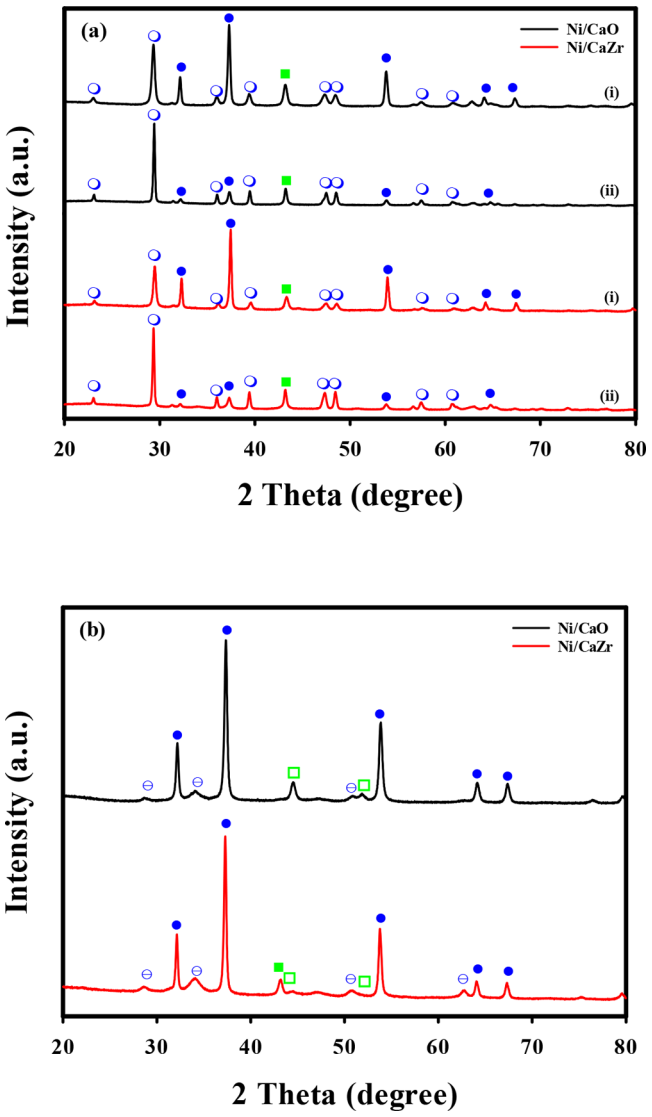

Figure 7. XRD patterns of Ni/CaO and Ni/CaZr DFMs after (a) (i) first and (ii) sixth carbonation and (b) fifth direct methanation in the ICCU process: (■) NiO and (□) Ni^0; (●) CaO, (○) $CaCO_3$, and (⊖) $CaOH_2$.

absorption of CO_2 at 500 °C for 2 h. It is also found that the NiO is reduced to the metallic Ni after direct methanation under H_2 conditions after the fifth direct methanation in Figure 7b. Then the Ni phase is converted back to the NiO phase by oxidizing metallic Ni by CO_2 or H_2O after the sixth CO_2 capture (Figure 7a).[9,10] In addition, the $CaCO_3$ phase was regenerated by direct methanation into the $CaO/Ca(OH)_2$ phases, as shown in Figure 7b. For Ni/CaO and Ni/CaZr DFMs, the conversion of CaO to $CaCO_3$ increased after sixth CO_2 capture cycles, which may be due to redispersion of the CaO phase.

In SEM images (Figure 8a,b), interconnected particles remained unchanged without severe aggregation in the Ni/CaO. In contrast, the cylindrical-like particles observed in the as-prepared sample were aggregated in the Ni/CaZr after five cycles of ICCM because of high conversion and volume expansion of CaO to $CaCO_3$ and longer time for reactions in the Ni/CaZr. Nevertheless, the macroporous structures remained unchanged, which resulted in stable CO_2 capture performance during five cycles of ICCM. In the TEM image, the crystallite size of Ni species in the Ni/CaO increased from 28.4 to 37.8 nm after five consecutive cycles of CO_2 capture and direct methanation (Figure 8c,e). Although a long time was required for CO_2 capture and direct methanation, the crystallite size of Ni species in Ni/CaZr DFM after five cycles of CO_2 capture and direct methanation is 18.9 nm (Figure 8d,f), which is smaller than that of NiO (26.9 nm) in the as-prepared state (Figure 3d,f). The decrease in the crystallite size is mainly attributed to the partial reduction of NiO to Ni^0 during methanation. The stronger interaction between Ni species and $CaZrO_3$ leads to the conclusion that adding ZrO_2 improves the inter-resistance of Ni nanoparticles.

As mentioned above, CH_4 productivity in the ICCM is directly related to the CO_2 capture capacity because all captured CO_2 in the carbonation step is converted to CH_4 during the direct methanation step. Therefore, thermal stability is one of the important factors affecting CH_4 productivity during the ICCM. CaO sintering-induced decrease in CO_2 capture capacity of the Ni/CaO and Ni/CaZr DFMs were investigated under conventional carbonation and decarbonation (Figure S10) and carbonation and direct methanation (Figure S11). Ni/CaZr DFM exhibited relatively stable CO_2 capture capacity under both conditions compared to Ni/CaO DFM. Based on these results, the Zr species acts as a barrier material in the intraregion of CaO, suppressing the CaO sintering during CO_2 capture and direct methanation at 500 °C.

3.5. *In Situ* DRIFTS Evaluation of ICCM. To identify the surface species on the Ni/CaZr DFMs during carbonation, desorption, and direct methanation, *in situ* DRIFTS spectra were evaluated, and product gases were analyzed in MS. Figure 9 shows the *in situ* DRIFTS spectra on performing carbonation (CO_2)−purge (He)−direct methanation (H_2) sequences over the Ni/CaZr DFM at 500 °C. During the carbonation step, the *in situ* DRIFTS spectra over the Ni/CaZr showed intense IR bands of the gaseous linearly adsorbed CO_2 at 2356 and 2316 cm^{-1} accompanied by the overtone at 3800−3500 cm^{-1}.[8,43,44] The peaks at 2960, 2868, 2580, 2500, 1794, 1343, 1097, 998, 884, and 859 cm^{-1} correspond to the absorption bands of bulk calcite ($CaCO_3$) species.[8] The sharp peaks at 1560, 1480, and 1350 cm^{-1} correspond to monodentate carbonate ($*CO_3$) on the CaO surface.[8,43] Monodentate carbonate species were assumed to be stable species adsorbed on strong basic sites (e.g., CaO). The broad peak at 1165−1300 cm^{-1} is assigned to O−H bending vibration of bicarbonate ($*HCO_3$), which formed from the CO_2 chemisorption on hydroxyl groups.[45] Several bands are attributed to formate species: symmetric and asymmetric vibration of O−C−O at 1580 and 1520 cm^{-1}, respectively, and the C−H stretching mode of formate at 2984 and 2923 cm^{-1}.[45] The weak peaks of polydentate carbonate on the ZrO_2 surface were observed at 1449 and 1426 cm^{-1}, but they are not dominant surface carbonate species.[8] The absorption band of nickel carbonyl at 2126 cm^{-1}, the doublet absorption bands of gaseous CO at 2180 and 2110 cm^{-1}, and bridged CO on Ni at 1930 cm^{-1} were observed, implying the dissociation of CO_2(ad) to CO(ad) and O(ad) on the surface of Ni metal.[8,46,47] It is also observed that the CO gas is produced from CO_2 dissociation or splitting initially in the MS

https://doi.org/10.1021/acs.energyfuels.3c02935
Energy Fuels 2023, 37, 19680−19694

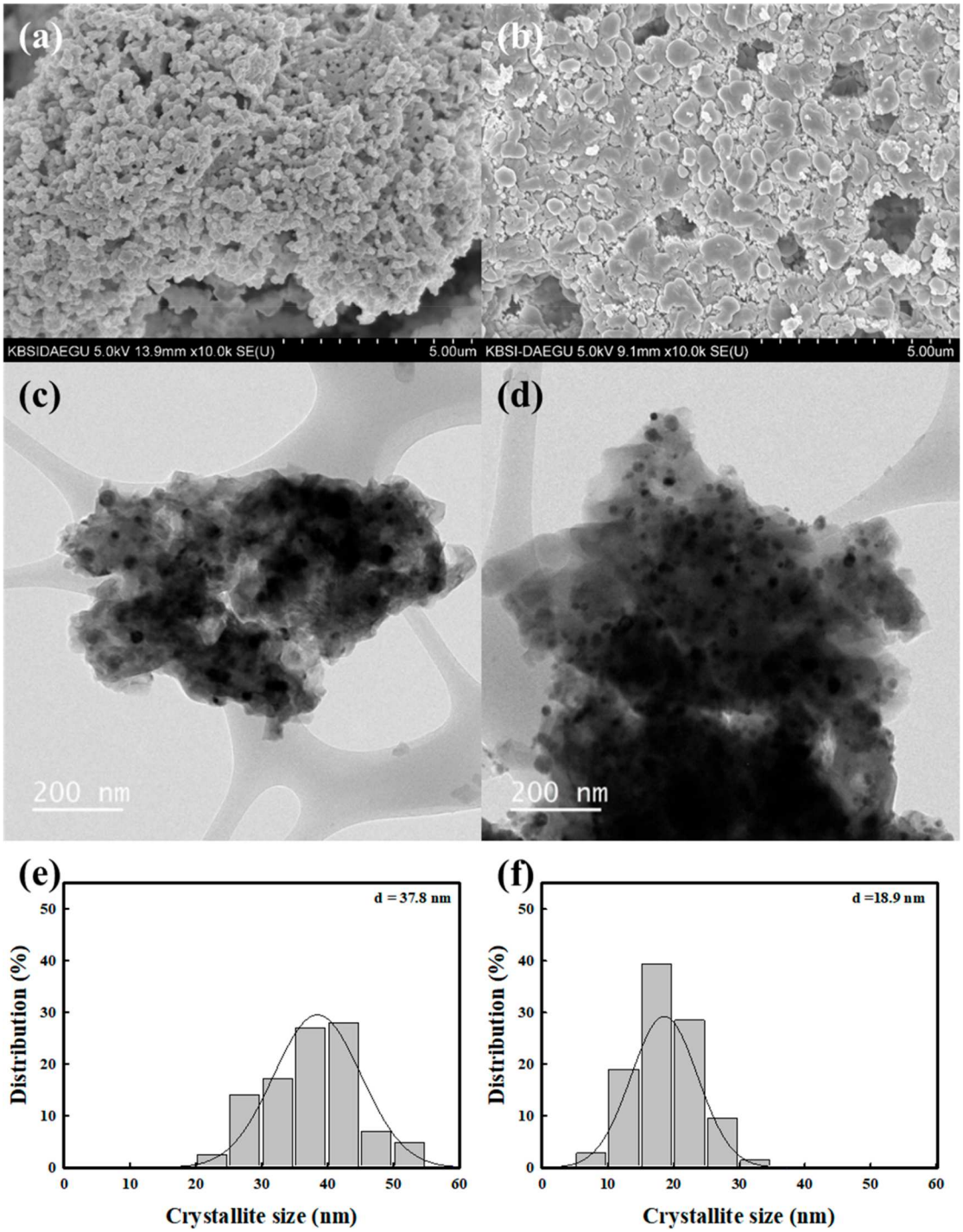

Figure 8. SEM images, TEM images, and Ni crystallite size of the (a, c, e) Ni/CaO and (b, d, f) Ni/CaZr DFMs after five cycles of CO_2 capture and direct methanation in ICCU.

spectra (Figure S12), and Ni is oxidized to NiO during the carbonation as observed in XRD result (Figure 9). Bulk calcite, surface carbonate, bicarbonate, formate, and CO adsorbed on Ni peaks increased with carbonation time. During the purge step, the gaseous linearly adsorbed CO_2 and overtone peaks at 3800−3500 cm^{-1} disappeared within 5 min, whereas bulk calcite, surface carbonate, and bicarbonate remained unchanged, indicating no decarbonation at 500 °C.

During the direct methanation, the formation of methoxy (1160 and 1107 cm^{-1}),[43] gaseous CH_4 (3012 cm^{-1}),[8,44] and C−H stretching mode of CH_4 (2984, 2923, and 1305 cm^{-1})[45] were accompanied by reduction of the peak intensity in monodentate carbonates (1560 and 1350 cm^{-1}), bicarbonates (1150−1300 cm^{-1}), and formate (1580 and 1520 cm^{-1}), implying that CH_4 is produced from the hydrogenation of monodentate carbonate, bicarbonates, and formate adsorbed on the CaO through the methoxy intermediate.[48] In addition, CO adsorbed on Ni (2120 cm^{-1}) and gaseous CO (2180 and 2070 cm^{-1}) were observed during the direct methanation, suggesting that the CO_2 adsorbed on CaO surface as monodentate carbonates are reduced to CO on the Ni surface.[48] The calcite peak also decreased slightly with

https://doi.org/10.1021/acs.energyfuels.3c02935
Energy Fuels 2023, 37, 19680−19694

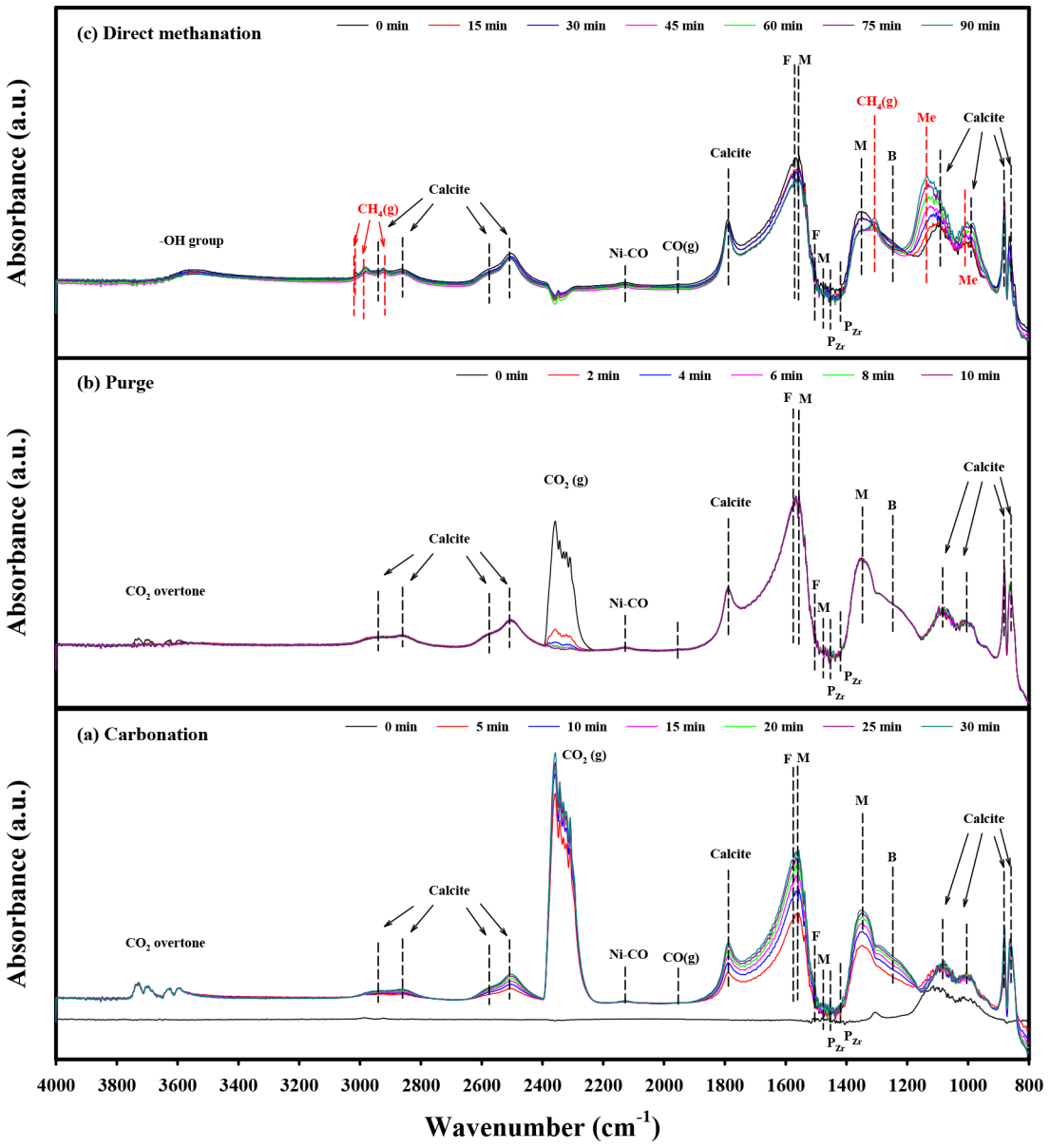

Figure 9. *In situ* DRIFTS spectra of (a) carbonation, (b) purge, and (c) direct methanation Ni/CaZr DFMs at 500 °C: (F) formate on CaO surface, (M) monodentate carbonates on CaO surface, (B) bicarbonates on CaO surface, (P_{Zr}) polydentate carbonate on ZrO_2 surface, and (Me) methoxy.

increasing reaction time because of its slow direct methanation kinetics. Therefore, it is concluded that CH_4 is produced through both routes: (1) formate and methoxy intermediate route on the CaO surface and (2) CO intermediate on the Ni surface.

Therefore, based on the experimental data, structural studies, and *in situ* DRIFTS studies, the mechanism in CO_2 capture and direct methanation in the ICCU process over Ni/CaO-based DFMs were proposed in Figure 10. During the CO_2 capture step, CO_2 as a Lewis acid, whose positive center is on the carbon atom, accepts the electron lone pairs, which presents on the oxide ion (O^{2-}) from CaO as a Lewis base, resulting in the formation of monodentate carbonates and bulk calcite. In addition, CO_2 is dissociated into carbonyl (CO_{ad}) and oxygen (O_{ad}) on the surface of Ni to produce NiO and CO gas during CO_2 capture. During the purge step, monodentate carbonates adsorbed on CaO and oxygen adsorbed on Ni were not desorbed under inert gas conditions (He). During the direct methanation step, oxidized Ni is first reduced by dissociated H_2 (Ni hydrides). The monodentate carbonates are converted to CH_4 via two routes: (1) bicarbonate, formate, and methoxy route on the CaO surface and (2) carbonyl route on the Ni−CaO interface. In route 1, monodentate carbonates are hydrogenated by dissociated H_2 to bicarbonate (HCO_{3ad}, 1a). Bicarbonates are dehydrated quickly to formate ($HCOO_{ad}$, 1b), followed by hydrogenation to methoxy (OCH_{3ad}, 1c). CH_4 is produced from successive hydrogenation of formate and methoxy intermediates (1d). In route 2, C and O atoms in carbonate species adsorb on the Ni surface, and hydrides added to carbonates to bicarbonates (carbonates spill over, 2a). Bicarbonates are dehydrated to formate species (b) and further dehydrated to carbonyl (2c). Carbonyl on the surface of Ni is not desorbed but hydrogenated to CH_4 at a relatively low temperature of 500

https://doi.org/10.1021/acs.energyfuels.3c02935
Energy Fuels 2023, 37, 19680−19694

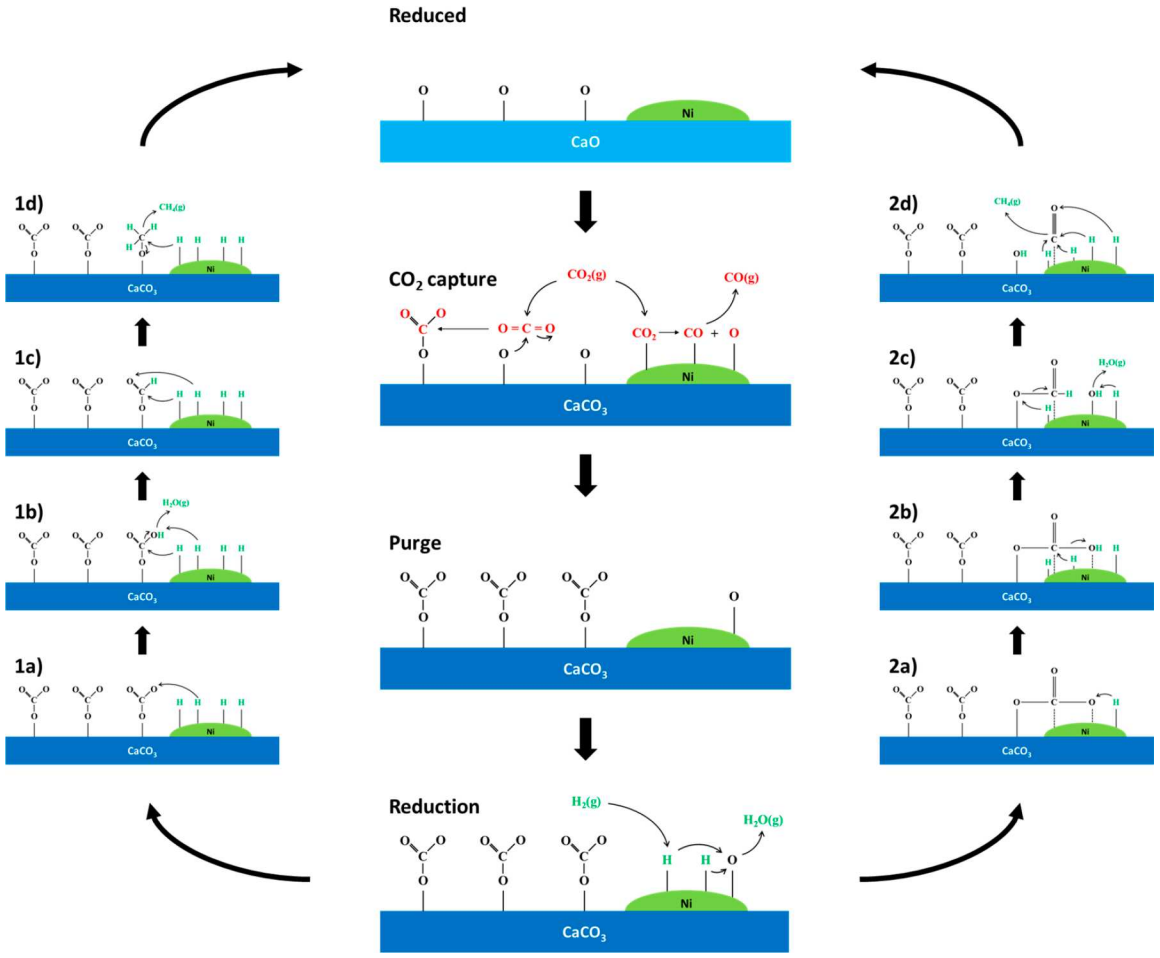

Figure 10. Proposed integrated CO_2 capture and direct methanation over Ni/CaO-based DFMs.

°C. Direct methanation by two routes is assumed to occur over adjacent Ni catalysts at the CaO/$CaCO_3$ interface of particle without sintering. In addition, CO_3^{2-} ions may diffuse outwardly from bulk calcite ($CaCO_3$) to CaO as a monodentate carbonate to produce CH_4. As direct methanation progresses, the radius of the unreacted $CaCO_3$ core in the particle decreases, leading to the complete $CaCO_3$ regeneration to CaO.

4. CONCLUSION

In this study, Zr-modified Ni/CaO (Ni/CaZr) DFM was prepared by the sol−gel method to determine the influence of Zr addition on its physicochemical properties and CO_2 capture and direct methanation performances. Adding a small amount of ZrO_2 (~2 wt %) to Ni/CaO DFM improved the macroporous structure of materials and the Ni dispersion throughout the CaO phase. The CO_2 capture kinetics increased at 500 °C with Zr addition due to the improvement of macroporous structures, thus enabling the diffusion of CO_2 into CaO through the thick layer of $CaCO_3$. In addition, the catalytic activity in CO_2 hydrogenation is enhanced because of better Ni dispersion by Zr addition. Ni/CaO and Ni/CaZr exhibited high CO_2 capture capacity and 100% CH_4 selectivity without CO_2 desorption at 500 °C during the five cycles of CO_2 capture and subsequent direct methanation. Moreover, Ni/CaZr DFMs achieved the highest CO_2 capture (13−14 mmol CO_2/g) and CH_4 productivity (13−14 mmol CH_4/g) at 500 °C compared to the CaO-based DFM or sorbent materials reported previously. CH_4 productivity is directly related to the CO_2 capture capacity because all of the CO_2 captured by CaO is converted to CH_4. It was revealed by *in situ* DRIFTS that CH_4 is produced in two ways: (1) formate and methoxy intermediate routes on the CaO surface and (2) CO intermediate on the Ni surface. The multicycle stability test of the CO_2 capture capacity was evaluated, and the Ni/CaZr DFMs showed superior thermal stability and stable CO_2 capture capacity in carbonation/decarbonation and carbonation/methanation.

■ ASSOCIATED CONTENT

Supporting Information

The Supporting Information is available free of charge at https://pubs.acs.org/doi/10.1021/acs.energyfuels.3c02935.

Textural properties measured by N_2 adsorption−desorption isotherms of the Ni/CaO and Ni/CaZr DFMs (Table S1); summary of CO_2 capture and direct methanation performance of Ni/CaO and Ni/CaZr DFMs (Tables S2 and S3); SEM images of the CaO and CaZr sorbents (Figure S1); TEM-EDS mapping of the Ni/CaO and Ni/CaZr (Figures S2 and S3); TEM-EDS analysis of the Ni/CaZr DFM (Figure S4); enlarged local XRD patterns of as-prepared Ni/CaZr DFM (Figure S5); equilibrium CO_2 partial pressure of CaO/$CaCO_3$ as a function of temperature (Figure S6); CH_4 and CO selectivity at equilibrium state in CO_2

https://doi.org/10.1021/acs.energyfuels.3c02935
Energy Fuels 2023, 37, 19680−19694

hydrogenation (H_2/CO_2 ratio = 1) as a function of temperature (Figure S7); H_2 conversion of Ni/CaO and Ni/CaZr DFMs during the direct methanation step (Figure S8); weight percent change of the CaO sorbent and Ni/CaO DFM under N_2 and H_2 conditions after carbonation (Figure S9); cyclic stability tests of the Ni/CaO and Ni/CaZr DFM in conventional carbonation and decarbonation (Figure S10); cyclic stability tests of the Ni/CaO and Ni/CaZr DFM under carbonation and direct methanation (Figure S11); mass spectra during the *in situ* DRIFTS experiment of carbonation (Figure S12) (PDF)

AUTHOR INFORMATION

Corresponding Authors

Jae Chang Kim − *Department of Chemical Engineering, Kyungpook National University, Daegu 41566, Republic of Korea;* orcid.org/0000-0003-2172-2881; Email: kjchang@knu.ac.kr

Soo Chool Lee − *Research Institute of Advanced Energy Technology, Kyungpook National University, Daegu 41566, Republic of Korea*; Email: soochool@knu.ac.kr

Kandis Leslie Gilliard-AbdulAziz − *Department of Chemical and Environmental Engineering, University of California, Riverside, Riverside, California 92521, United States; Sonny Astani Department of Civil and Environmental Engineering, University of Southern California, Los Angeles, California 90089, United States;* orcid.org/0000-0002-1706-9552; Email: klabdulaziz@engr.ucr.edu

Authors

Seongbin Jo − *Department of Chemical and Environmental Engineering, University of California, Riverside, Riverside, California 92521, United States;* orcid.org/0000-0002-6622-3616

Jin Hyeok Woo − *Department of Chemical Engineering, Kyungpook National University, Daegu 41566, Republic of Korea*

Tu Nguyen − *Department of Chemical and Environmental Engineering, University of California, Riverside, Riverside, California 92521, United States;* orcid.org/0000-0002-7423-143X

Ju Eon Kim − *Department of Chemical Engineering, Kyungpook National University, Daegu 41566, Republic of Korea*

Tae Young Kim − *Research Institute of Advanced Energy Technology, Kyungpook National University, Daegu 41566, Republic of Korea*

Ho-Jung Ryu − *Korea Institute of Energy Research, Daejeon 34129, Republic of Korea*

Byungwook Hwang − *Korea Institute of Energy Research, Daejeon 34129, Republic of Korea*

Complete contact information is available at: https://pubs.acs.org/10.1021/acs.energyfuels.3c02935

Author Contributions

S.J. and J.H.W. contributed equally to this work.

Notes

The authors declare no competing financial interest.

ACKNOWLEDGMENTS

This work was supported by the Korea Institute of Energy Technology Evaluation and Planning (KETEP) and the Ministry of Trade, Industry & Energy (MOTIE) of the Republic of Korea (20213030030240) and partially supported by the National Science Foundation (CBET: No. 2143578). We are grateful for the financial support.

REFERENCES

(1) Woo, J.-H.; Jo, S.; Kim, J.-E.; Kim, T.-Y.; Son, H.-D.; Ryu, H.-J.; Hwang, B.; Kim, J.-C.; Lee, S.-C.; Gilliard-AbdulAziz, K. L. Effect of the Ni-to-CaO Ratio on Integrated CO_2 Capture and Direct Methanation. *Catalysts* **2023**, *13* (8), 1174.

(2) Al-Mamoori, A.; Hameed, M.; Saoud, A.; Al-ghamdi, T.; Al-Naddaf, Q.; ALwakwak, A.-A.; Baamran, K. Development of Sodium-Based Borate Adsorbents for CO_2 Capture at High Temperatures. *Ind. Eng. Chem. Res.* **2023**, *62* (8), 3695−3704.

(3) Sun, H.; Zhang, Y.; Wang, C.; Isaacs, M. A.; Osman, A. I.; Wang, Y.; Rooney, D.; Wang, Y.; Yan, Z.; Parlett, C. M.A.; Wang, F.; Wu, C. Integrated carbon capture and utilization: Synergistic catalysis between highly dispersed Ni clusters and ceria oxygen vacancies. *Chem. Eng. J.* **2022**, *437*, 135394.

(4) Lawson, S.; Baamran, K.; Newport, K.; Rezaei, F.; Rownaghi, A. A. Formulation and processing of dual functional Adsorbent/Catalyst structured monoliths using an additively manufactured contactor for direct Capture/Conversion of CO_2 with cogeneration of ethylene. *Chem. Eng. J.* **2022**, *431*, 133224.

(5) Jo, S.; Lee, J. H.; Woo, J. H.; Kim, T.-Y.; Ryu, H.-J.; Hwang, B.; Kim, J. C.; Lee, S. C.; Gilliard-AbdulAziz, K. L. Coke-promoted Ni/CaO catal-sorbents in the production of cyclic CO and syngas. *Sustainable Energy & Fuels* **2021**, *6* (1), 81−88.

(6) Jo, S.; Cruz, L.; Shah, S.; Wasantwisut, S.; Phan, A.; Gilliard-AbdulAziz, K. L. Perspective on Sorption Enhanced Bifunctional Catalysts to Produce Hydrocarbons. *ACS Catal.* **2022**, *12* (13), 7486−7510.

(7) Jeong-Potter, C.; Farrauto, R. Feasibility study of combining direct air capture of CO_2 and methanation at isothermal conditions with dual function materials. *Appl. Catal. B: Environmental* **2021**, *282*, 119416.

(8) Hu, J.; Hongmanorom, P.; Galvita, V. V.; Li, Z.; Kawi, S. Bifunctional Ni-Ca based material for integrated CO_2 capture and conversion via calcium-looping dry reforming. *Appl. Catal. B: Environmental* **2021**, *284*, 119734.

(9) Jo, S. B.; Woo, J. H.; Lee, J. H.; Kim, T. Y.; Kang, H. I.; Lee, S. C.; Kim, J. C. A novel integrated CO 2 capture and direct methanation process using Ni/CaO catal-sorbents. *Sustainable Energy & Fuels* **2020**, *4* (9), 4679−4687.

(10) Jo, S. B.; Woo, J. H.; Lee, J. H.; Kim, T. Y.; Kang, H. I.; Lee, S. C.; Kim, J. C. CO 2 green technologies in CO 2 capture and direct utilization processes: methanation, reverse water-gas shift, and dry reforming of methane. *Sustainable Energy & Fuels* **2020**, *4* (11), 5543−5549.

(11) Al-Mamoori, A.; Lawson, S.; Rownaghi, A. A.; Rezaei, F. Oxidative dehydrogenation of ethane to ethylene in an integrated CO_2 capture-utilization process. *Appl. Catal. B: Environmental* **2020**, *278*, 119329.

(12) Al-Mamoori, A.; Rownaghi, A. A.; Rezaei, F. Combined capture and utilization of CO_2 for syngas production over dual-function materials. *ACS Sustainable Chem. Eng.* **2018**, *6* (10), 13551−13561.

(13) Jo, S.; Son, H. D.; Kim, T.-Y.; Woo, J. H.; Ryu, D. Y.; Kim, J. C.; Lee, S. C.; Gilliard-AbdulAziz, K. L. Ru/K2CO3-MgO catalytic sorbent for integrated CO_2 capture and methanation at low temperatures. *Chem. Eng. J.* **2023**, *469*, 143772.

(14) Ho, H.-J.; Iizuka, A.; Shibata, E. Carbon capture and utilization technology without carbon dioxide purification and pressurization: a review on its necessity and available technologies. *Ind. Eng. Chem. Res.* **2019**, *58* (21), 8941−8954.

(15) Varvoutis, G.; Lykaki, M.; Stefa, S.; Binas, V.; Marnellos, G. E.; Konsolakis, M. Deciphering the role of Ni particle size and nickel-ceria interfacial perimeter in the low-temperature CO_2 methanation reaction over remarkably active Ni/CeO_2 nanorods. *Appl. Catal. B: Environmental* **2021**, *297*, 120401.
(16) Morgenthaler, S.; Ball, C.; Koj, J. C.; Kuckshinrichs, W.; Witthaut, D. Site-dependent levelized cost assessment for fully renewable Power-to-Methane systems. *Energy conversion and management* **2020**, *223*, 113150.
(17) Li, W.; Nie, X.; Jiang, X.; Zhang, A.; Ding, F.; Liu, M.; Liu, Z.; Guo, X.; Song, C. ZrO2 support imparts superior activity and stability of Co catalysts for CO_2 methanation. *Appl. Catal. B: Environmental* **2018**, *220*, 397−408.
(18) Frontera, P.; Macario, A.; Ferraro, M.; Antonucci, P. Supported catalysts for CO_2 methanation: a review. *Catalysts* **2017**, *7* (2), 59.
(19) Guilera, J.; del Valle, J.; Alarcon, A.; Díaz, J. A.; Andreu, T. Metal-oxide promoted Ni/Al2O3 as CO_2 methanation micro-size catalysts. *Journal of CO_2 Utilization* **2019**, *30*, 11−17.
(20) Zhan, Y.; Wang, Y.; Gu, D.; Chen, C.; Jiang, L.; Takehira, K. Ni/Al2O3-ZrO2 catalyst for CO_2 methanation: the role of γ-(Al, Zr) 2O3 formation. *Appl. Surf. Sci.* **2018**, *459*, 74−79.
(21) Lawson, S.; Baamran, K.; Newport, K.; Alghamadi, T.; Jacobs, G.; Rezaei, F.; Rownaghi, A. A. Integrated direct air capture and oxidative dehydrogenation of propane with CO_2 at isothermal conditions. *Appl. Catal. B: Environmental* **2022**, *303*, 120907.
(22) Wei, S.; Han, R.; Su, Y.; Gao, J.; Zhao, G.; Qin, Y. Pore structure modified CaO-based sorbents with different sized templates for CO_2 capture. *Energy Fuels* **2019**, *33* (6), 5398−5407.
(23) Yoon, H. J.; Lee, K. B. Introduction of chemically bonded zirconium oxide in CaO-based high-temperature CO_2 sorbents for enhanced cyclic sorption. *Chem. Eng. J.* **2019**, *355*, 850−857.
(24) Zhang, C.; Li, Y.; He, Z.; Zhao, J.; Wang, D. Microtubular Fe/Mn-promoted CaO-Ca12Al14O33 bi-functional material for H2 production from sorption enhanced water gas shift. *Appl. Catal. B: Environmental* **2022**, *314*, 121474.
(25) Jin, S.; Ko, K.-J.; Lee, C.-H. Direct formation of hierarchically porous MgO-based sorbent bead for enhanced CO_2 capture at intermediate temperatures. *Chem. Eng. J.* **2019**, *371*, 64−77.
(26) Teixeira, P.; Hipólito, J.; Fernandes, A.; Ribeiro, F.; Pinheiro, C. I. Tailoring synthetic sol-gel CaO sorbents with high reactivity or high stability for Ca-looping CO_2 capture. *Ind. Eng. Chem. Res.* **2019**, *58* (19), 8484−8494.
(27) Armutlulu, A.; Naeem, M. A.; Liu, H. J.; Kim, S. M.; Kierzkowska, A.; Fedorov, A.; Müller, C. R. Multishelled CaO microspheres stabilized by atomic layer deposition of Al2O3 for enhanced CO_2 capture performance. *Adv. Mater.* **2017**, *29* (41), 1702896.
(28) Salaudeen, S. A.; Acharya, B.; Dutta, A. CaO-based CO_2 sorbents: A review on screening, enhancement, cyclic stability, regeneration and kinetics modelling. *Journal of CO_2Utilization* **2018**, *23*, 179−199.
(29) Heidari, M.; Tahmasebpoor, M.; Antzaras, A.; Lemonidou, A. A. CO_2 capture and fluidity performance of CaO-based sorbents: effect of Zr, Al and Ce additives in tri-, bi-and mono-metallic configurations. *Process Safety and Environmental Protection* **2020**, *144*, 349−365.
(30) Azimi, B.; Tahmasebpoor, M.; Sanchez-Jimenez, P. E.; Perejon, A.; Valverde, J. M. Multicycle CO_2 capture activity and fluidizability of Al-based synthesized CaO sorbents. *Chem. Eng. J.* **2019**, *358*, 679−690.
(31) Krödel, M.; Landuyt, A.; Abdala, P. M.; Müller, C. R. Mechanistic Understanding of CaO-Based Sorbents for High-Temperature CO_2 Capture: Advanced Characterization and Prospects. *ChemSusChem* **2020**, *13* (23), 6259−6272.
(32) Zhao, C.; Zhou, Z.; Cheng, Z.; Fang, X. Sol-gel-derived, CaZrO3-stabilized Ni/CaO-CaZrO3 bifunctional catalyst for sorption-enhanced steam methane reforming. *Appl. Catal. B: Environmental* **2016**, *196*, 16−26.
(33) Le, T. A.; Kim, T. W.; Lee, S. H.; Park, E. D. CO and CO 2 methanation over Ni catalysts supported on alumina with different crystalline phases. *Korean Journal of Chemical Engineering* **2017**, *34*, 3085−3091.
(34) Nagu, A.; Vasikerappa, K.; Gidyonu, P.; Prathap, C.; Venkata Rao, M.; Rama Rao, K.; David Raju, B. Additive-free vapour-phase hydrogenation of benzonitrile over MgO-supported Ni catalysts. *Res. Chem. Intermed.* **2020**, *46*, 2669−2681.
(35) Yang, F.; Liu, D.; Zhao, Y.; Wang, H.; Han, J.; Ge, Q.; Zhu, X. Size dependence of vapor phase hydrodeoxygenation of m-cresol on Ni/SiO_2 catalysts. *ACS catalysis* **2018**, *8* (3), 1672−1682.
(36) Ye, R.-P.; Gong, W.; Sun, Z.; Sheng, Q.; Shi, X.; Wang, T.; Yao, Y.; Razink, J. J.; Lin, L.; Zhou, Z.; et al. Enhanced stability of Ni/SiO_2 catalyst for CO_2 methanation: Derived from nickel phyllosilicate with strong metal-support interactions. *Energy* **2019**, *188*, 116059.
(37) Hashemi, S. M.; Karami, D.; Mahinpey, N. CaO-Based Nanomaterials Promoted with CaZrO3 for High-Temperature Carbon Capture. *Ind. Eng. Chem. Res.* **2022**, *61* (16), 5514−5526.
(38) O'Connell, K.; Regalbuto, J. R. High sensitivity silicon slit detectors for 1 nm powder XRD size detection limit. *Catal. Lett.* **2015**, *145*, 777−783.
(39) Guo, H.; Wang, S.; Li, C.; Zhao, Y.; Sun, Q.; Ma, X. Incorporation of Zr into calcium oxide for CO_2 capture by a simple and facile sol-gel method. *Ind. Eng. Chem. Res.* **2016**, *55* (29), 7873−7879.
(40) Hu, Y.; Xu, Q.; Sheng, Y.; Wang, X.; Cheng, H.; Zou, X.; Lu, X. Catalytic Synthesis of CO by Combining CO_2 Capture and Hydrogenation over Three-Dimensional Ni/CaO Networks. *Energy Fuels* **2023**, *37*, 7871.
(41) Xu, Y.; Ding, H.; Luo, C.; Zhang, Q.; Zheng, Y.; Li, X.; Hu, Y.; Zhang, L. NaBr-enhanced CaO-based sorbents with a macropore-stabilized microstructure for CO_2 capture. *Energy Fuels* **2018**, *32* (8), 8571−8578.
(42) Xu, Y.; Luo, C.; Zheng, Y.; Ding, H.; Zhang, L. Macropore-stabilized limestone sorbents prepared by the simultaneous hydration-impregnation method for high-temperature CO_2 capture. *Energy Fuels* **2016**, *30* (4), 3219−3226.
(43) González-Rangulan, V. V.; Reyero, I.; Bimbela, F.; Romero-Sarria, F.; Daturi, M.; Gandía, L. M. CO_2Methanation over Nickel Catalysts: Support Effects Investigated through Specific Activity and Operando IR Spectroscopy Measurements. *Catalysts* **2023**, *13* (2), 448.
(44) Proaño, L.; Tello, E.; Arellano-Trevino, M. A.; Wang, S.; Farrauto, R. J.; Cobo, M. In-situ DRIFTS study of two-step CO_2 capture and catalytic methanation over Ru,"Na2O"/Al2O3 Dual Functional Material. *Appl. Surf. Sci.* **2019**, *479*, 25−30.
(45) Cárdenas-Arenas, A.; Quindimil, A.; Davó-Quiñonero, A.; Bailón-García, E.; Lozano-Castello, D.; De-La-Torre, U.; Pereda-Ayo, B.; González-Marcos, J. A.; González-Velasco, J. R.; Bueno-López, A. Isotopic and in situ DRIFTS study of the CO_2 methanation mechanism using Ni/CeO_2 and Ni/Al2O3 catalysts. *Appl. Catal. B: Environmental* **2020**, *265*, 118538.
(46) Das, S.; Ashok, J.; Bian, Z.; Dewangan, N.; Wai, M.; Du, Y.; Borgna, A.; Hidajat, K.; Kawi, S. Silica-Ceria sandwiched Ni core-shell catalyst for low temperature dry reforming of biogas: Coke resistance and mechanistic insights. *Appl. Catal. B: Environmental* **2018**, *230*, 220−236.
(47) Huynh, H. L.; Zhu, J.; Zhang, G.; Shen, Y.; Tucho, W. M.; Ding, Y.; Yu, Z. Promoting effect of Fe on supported Ni catalysts in CO_2 methanation by in situ DRIFTS and DFT study. *J. Catal.* **2020**, *392*, 266−277.
(48) Miao, B.; Ma, S. S. K.; Wang, X.; Su, H.; Chan, S. H. Catalysis mechanisms of CO 2 and CO methanation. *Catalysis Science & Technology* **2016**, *6* (12), 4048−4058.
(49) Sun, H.; Wang, J.; Zhao, J.; Shen, B.; Shi, J.; Huang, J.; Wu, C. Dual functional catalytic materials of Ni over Ce-modified CaO sorbents for integrated CO_2 capture and conversion. *Appl. Catal. B: Environmental* **2019**, *244*, 63−75.

https://doi.org/10.1021/acs.energyfuels.3c02935
Energy Fuels 2023, 37, 19680−19694

(50) Tian, S.; Yan, F.; Zhang, Z.; Jiang, J. Calcium-looping reforming of methane realizes in situ CO_2 utilization with improved energy efficiency. *Sci. Adv.* **2019**, *5* (4), No. eaav5077.
(51) Naeem, M. A.; Armutlulu, A.; Imtiaz, Q.; Donat, F.; Schäublin, R.; Kierzkowska, A.; Müller, C. R. Optimization of the structural characteristics of CaO and its effective stabilization yield high-capacity CO_2 sorbents. *Nat. Commun.* **2018**, *9* (1), 2408.
(52) Huang, L.; Zhang, Y.; Gao, W.; Harada, T.; Qin, Q.; Zheng, Q.; Hatton, T. A.; Wang, Q. Alkali carbonate molten salt coated calcium oxide with highly improved carbon dioxide capture capacity. *Energy Technology* **2017**, *5* (8), 1328−1336.

https://doi.org/10.1021/acs.energyfuels.3c02935
Energy Fuels 2023, 37, 19680−19694